RSC Advances

PAPER

View Article Online
View Journal | View Issue

Cite this: *RSC Adv.*, 2025, **15**, 8530

Synthesis, characterization, and luminescence thermometry investigation of $LiSrGd(WO_4)_3:Pr^{3+}$ phosphors

Refka Tahri,[a] Mouna Fhoula,[a] Fadwa Ayachi,[a] Tarak Koubaa,[a] Mohamed Dammak, *[a] Joan Josep Carvajal [b] and Maria Cinta Pujol[b]

In this study, $LiSrGd(WO_4)_3$ (LSGW) phosphors doped with different concentrations of Pr^{3+} were synthesized *via* the traditional solid–solid method to explore their suitability for luminescence thermometry applications. Structural and morphological analyses using X-ray powder diffraction and scanning electron microscopy offered comprehensive insights. The energy gap value of LSGW, calculated at $E_g = 3.69$ eV for $x = 5$ at% Pr^{3+}, suggested minimal alteration in the bandgap energy upon incorporation of Pr^{3+} ions into the LSGW host. The empirical energy levels for the free ion Pr^{3+} were derived from absorption and emission data are gathered from LSGW:Pr^{3+}. The theoretical energy diagram and corresponding eigenstates for Pr^{3+} were calculated using block diagonalization of the Hamiltonian's matrix in the basis set of coupled states $\langle 4f^2\rangle\langle 4f^2\tau SLJ\rangle$, considering intermediate coupling. Thermometric parameters were calculated using the luminescence intensity ratio strategy based on Pr^{3+} emission spectra for thermal coupled levels. Our findings revealed that the LIR1 (I_{531}/I_{557}) exhibited maximum absolute and relative sensitivities of 31.5 10^{-4} K^{-1} and 0.65% K^{-1}, respectively, at 300 K, accompanied by remarkably low-temperature uncertainty (δT) values ranging from 0.031 to 0.037 K in the 300–440 K temperature range. These results show the importance of $LiSrGd(WO_4)_3:Pr^{3+}$ phosphors for optical applications.

Received 2nd January 2025
Accepted 13th March 2025

DOI: 10.1039/d5ra00039d

rsc.li/rsc-advances

1. Introduction

Optical temperature sensors have recently received significant attention due to their potential applications in inaccessible, harsh, or hazardous environments.[1–3] Recently, considerable focus has been given to contactless luminescence thermometry, which represents a new technique enabling temperature measurement with submicron spatial resolution and sub degree thermal precision.[4–6] The luminescence (fluorescence) intensity ratio technique, known as LIR (FIR), is widely employed for optical temperature detection due to its quick measurement capability, high thermal resolution, and excellent precision.[7,8] The LIR method exploits the temperature-induced variations in the intensity ratio of emission bands linked to the thermally-coupled levels (TCLs) of various lanthanide (Ln) ions. The energy separation (ΔE) between their TCLs ranges approximately from 200 to 2000 cm^{-1}.[9,10]

Trivalent praseodymium (Pr^{3+}) stands out among activator Ln ions for its fluorescence spanning from the ultraviolet, to the visible and near-infrared wavelengths. Its emission characteristics include green-bluish and red light, attributed to transitions within the $^3P_{0,1}$ and $^1D_2$ multiplets.[11–13] The incorporation of Pr^{3+} into phosphors has demonstrated notable sensing capabilities, enabled by cross relaxation (CR) processes between the $^3P_0$ and $^1D_2$ levels or between the thermally coupled levels (TCLs) $^3P_0$ and $^3P_1$. Additionally, researchers have investigated the interference of the metal–metal intervalence charge transfer (IVCT) state with Pr^{3+} luminescence as an innovative strategy for designing high-performance FIR-based thermometers. Previous studies have harnessed different Pr^{3+} transitions for FIR calculations based on their temperature-dependent intensity variations.[14–22]

For the design of highly efficient luminescent materials and sensors, the choice of a suitable host material is crucial. Specially, tungstate has a strong and broad charge transfer band in the near-ultraviolet region due to the $(WO_4)_2$ group. This allows it to enhance the luminescence of the fluorescent activation centre by absorbing near-ultraviolet energy and transferring it to the light emitting centre.[23–25] Furthermore, tungstate compounds serve as excellent hosts for photoactive lanthanide ions, with potential applications in phosphors, lasers, photocatalysis, and negative thermal expansion.[26,27] Numerous reports exist in the literature on tungstates, particularly those involving rare earth ions such as Sm, Ce, and Tm, there is a noticeable gap in research focused specifically on $LiSrGd(WO_4)_3$ hosts. This particular compound remains

[a]*Laboratoire de Physique Appliquée, Faculté des Sciences de Sfax, Département de Physique, Université de Sfax, BP 1171, Sfax, Tunisia. E-mail: madidammak@yahoo.fr; mohamed.dammak@fss.usf.tn*

[b]*Universitat Rovira i Virgili, Departament de Química Física i Inorgànica, Materials in Green Chemistry (GreenMat), Marcel·li Domingo 1, Tarragona 43007, Spain*

relatively understudied compared to its counterparts. The $LiSrGd(WO_4)_3$ structure is intriguing as it exhibits two polymorphic forms, transitioning between a monoclinic structure at low temperatures and an orthorhombic structure at higher temperatures, influenced primarily by the electronegativity of the rare earth ion.[28] $Gd_2(WO_4)_3$, a member of the rare earth tungstate family, holds particular significance due to its versatility and applications in various fields including optical fibers, sensors, scintillators, light-emitting diodes, and solid-state lasers.[29] While $Gd_2(WO_4)_3$ and its substitutions have been extensively investigated for their optical properties, including self-luminescence in the visible spectrum, there is a notable gap in research specifically addressing the $LiSrGd(WO_4)$ host.

This paper focuses on the synthesis and characterizations of $LiSrGd(WO_4)_3$:Pr^{3+} phosphors, with a notable emphasis on luminescent thermometry investigation. It begins with a detailed account of the synthesis process, followed by comprehensive characterizations including structural, morphological, and spectroscopic analyses. Results and discussions delve into various aspects such as structural and morphological characteristics, FTIR, UV-visible spectrum, photoluminescence, theoretical simulations of energy levels of free Pr^{3+} ion, and luminescence thermal stability with a specific focus on CIE changes in UC with temperature.

The study of luminescent thermometry explores the feasibility and accuracy of using luminophores for temperature sensing, highlighting their potential applications in advanced temperature measurement technologies.

2. Experimental section and characterizations

$LiSrGd_{1-x}(WO_4)_3$:x% Pr^{3+} (x = 1, 3, 5, and 7 at%) were synthesized though the traditional solid-state reaction method. High-purity precursors (≥99%) including lithium carbonate (Li_2CO_3), strontium carbonate ($SrCO_3$), praseodymium oxide (Pr_6O_{11}), gadolinium oxide (Gd_2O_3) and tungsten oxide (WO_3) were mixed in stoichiometric proportions and ground into fine powders. The mixture was then placed in a crucible and heated up to 350 °C for 10 hours. After cooling, the resulting product was then weighed, manually crushed, and pressed into pellets. These pellets were sintered at 800 °C for 5 hours. The particle agglomeration was observed during the sintering process at 800 °C, where increased atomic diffusion promotes grain growth and particle coalescence. The synthesis of the $LiSrGd_{1-x}Pr_x(WO_4)_3$ compound can be described by the following reaction:

$$3Li_2CO_3 + 6SrCO_3 + 3(1 - x)Gd_2O_3 + xPr_6O_{11} + 9W_2O_3 + (18 - 4x)O_2 \rightarrow 6LiSrGd_{1-x}Pr_x(WO_4)_3 + 9CO_2$$

A Siemens-D8-$\theta/2\theta$ diffractometer with a Cu Kα X-ray source (λ = 0.15418 nm) was employed for X-ray diffraction (XRD) measurements under grazing incidence. A Thermo Scientific Apreo 2 S LoVac field emission scanning electron microscope (FE-SEM) is used to study the morphology of the samples. The Fourier transform infrared (FT-IR) spectra of the material were obtained at room temperature within the 400–4000 cm^{-1} range using a PerkinElmer 1000 FTIR spectrometer. UV-vis-NIR absorption was measured using a PerkinElmer Lambda 365 UV-vis-NIR spectrometer. Photoluminescence spectra were measured using a Fluoromax 4P model Horiba spectrometer with a xenon arc lamp as the excitation source. Temperature-dependent DC emission was examined using a JOBIN YVON HR 320 spectrometer fitted with a temperature controller and a 450 nm laser excitation source.

3. Results and discussion

3.1. XRD and SEM

The XRD patterns of praseodymium doped LSGW synthesized in this work are shown in Fig. 1. All samples are crystalline. Most of the peaks can be assigned to the tetragonal scheelite crystalline phase, with the space group $I4_1/a$ (no. 88).[30] Small diffraction peaks can be observed at $2\theta = 13.39°$ and $2\theta = 14.4°$, which should belong to the oxide precursors. In this crystal, Li, Sr, Gd and Pr^{3+} are distributed randomly in the S_4 site that in $CaWO_4$ occupies Ca^{2+}; which is surrounded by 8 oxygens. It was possible to clearly observe the shift of the peak located at around 18°, corresponding to the (101) reflection and shown in the inset of Fig. 1, when the Pr^{3+} concentration increased.

Table 1 summarizes the unit cell parameters refined by using the Le Bail methodology using the TOPAS software. The introduction of Pr^{3+} in the crystalline structure affects the unit cell parameters, showing first a slight decrease in size for the two parameters a and c, that for Pr^{3+} concentrations of 5 at% or higher, increased again. This compression/stress should be expected when substituting Gd^{3+} or Sr^{2+} by Pr^{3+} because of the difference in ionic radii in a coordination environment of 8, that is Gd^{3+} = 1.05 Å, Pr^{3+} = 0.99 Å and Sr^{2+} = 1.18 Å. According to these data, a hypothesis that can be established is that Pr^{3+} tends to substitute first Sr^{2+} in the structure at low concentrations (below 5 at%), but then, as the concentration increases, it tends to substitute also Gd^{3+}. However, no experiments have been done to confirm this.[31,32]

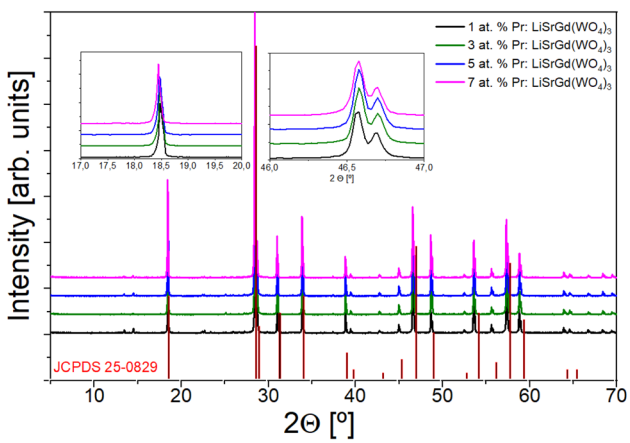

Fig. 1 XRD patterns of the obtained products, $LiSrGd(WO_4)_3$:x at% Pr^{3+} (x = 1, 3, 5, and 7). Inset: angle shift of the (101) reflection related to the Pr concentration.

Table 1 Evolution of the unit cell parameters as a function of the doping level

% Pr	a (Å)	c (Å)	Volume (Å^3)	R_{exp}/R_{wp}
1	5.28683	11.53198	322.326	5.43/24.96
3	5.28671	11.52927	322.235	5.14/19.50
5	5.28710	11.53043	322.314	5.10/15.70
7	5.28845	11.53205	322.525	5.10/11.73

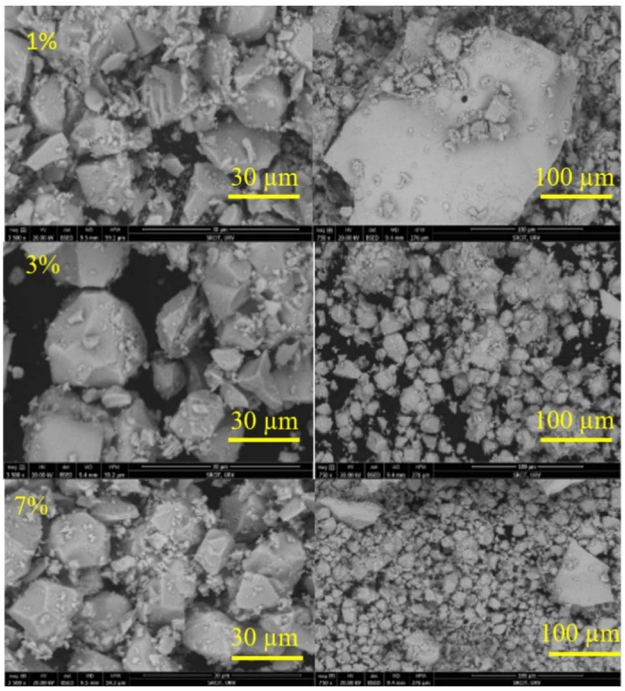

Fig. 2 SEM micrographs of LSGW:x at% Pr^{3+} (x = 1, 3, and 5) recorded at two different sizes.

The observed shift of diffraction peaks toward higher 2θ angles compared to the standard JCPDS data can be attributed to the substitution of Gd^{3+} and/or Sr^{2+} by Pr^{3+} in the $LiSrGd(WO_4)_3$ lattice. This substitution induces a slight contraction of the unit cell, leading to peak shifts according to Bragg's law. Additionally, minor structural strain introduced during the solid-state synthesis process could further contribute to these shifts. Such peak displacements are commonly observed in doped phosphor systems and reflect changes in lattice parameters due to ionic substitution.

Fig. 2 shows the microstructure of LSGW particles doped with (1, 3, 5)% Pr^{3+} obtained at two different sizes (30 and 100 μm). Irregularly shaped particles, approximately 10 μm in size, are observed. Moreover, high-temperature heat treatments result in significant particle agglomeration.

3.2. FTIR spectroscopy

Fig. 3 shows the FTIR spectra of LSGW:3 at% Pr^{3+} and LSGW:5 at% Pr^{3+} phosphors. The set of vibrational bands below 1000 cm^{-1} belong to the characteristic absorption of WO_4^{2-}

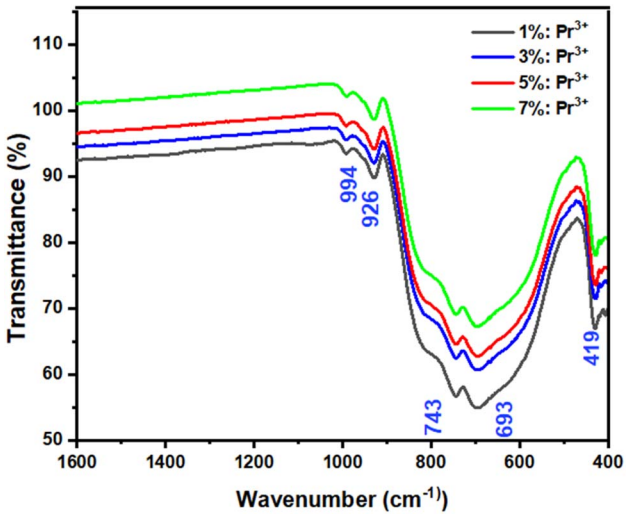

Fig. 3 FTIR spectra of LSGW:x at% Pr^{3+} (x = 1, 3, 5, and 7).

group.[33] The absorption peaks at 994 cm^{-1} and 926 cm^{-1} are ascribed to the stretching mode of the W=O and W–O bands, respectively.[34,35] The peaks at 820 and 419 cm^{-1} is attributed to the stretching and bending modes of single WOW bridge, while the absorption peaks at 743 and 693 cm^{-1} are related to the stretching mode of the double WOOW bridge.[34] Thus, the results of FTIR analysis further prove the formation of LSGW.

3.3. Optical characterization

UV-visible spectroscopy. Fig. 4 shows the UV-visible reflectance spectra of LSGW:x at% Pr^{3+} in the 200–1000 nm range. In all the spectra, there's a broad absorption band in the UV range (200–400 nm) which is assigned to the W–O charge transfer band (CTB), involves electron transitions from the 2p oxygen orbital to the 4d tungsten orbital.[36] The 4f–4f intrinsic transitions of the Pr^{3+} ion are located around 448 nm, 475 nm, 488 nm

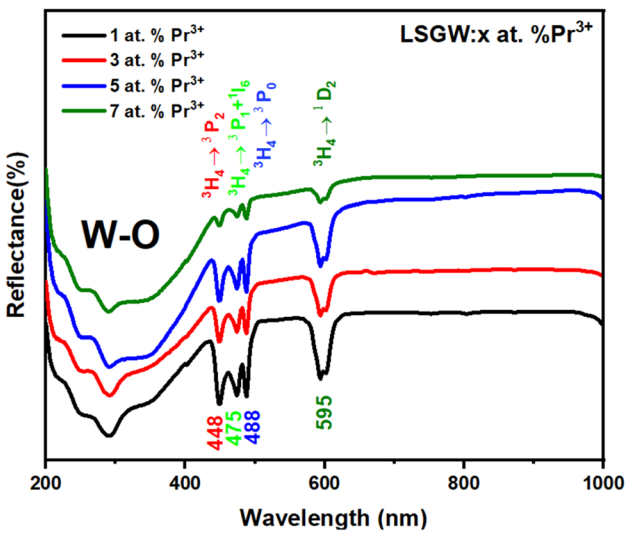

Fig. 4 Reflectance spectra of LSGW:x at% Pr^{3+} (x = 1, 3, 5, and 7).

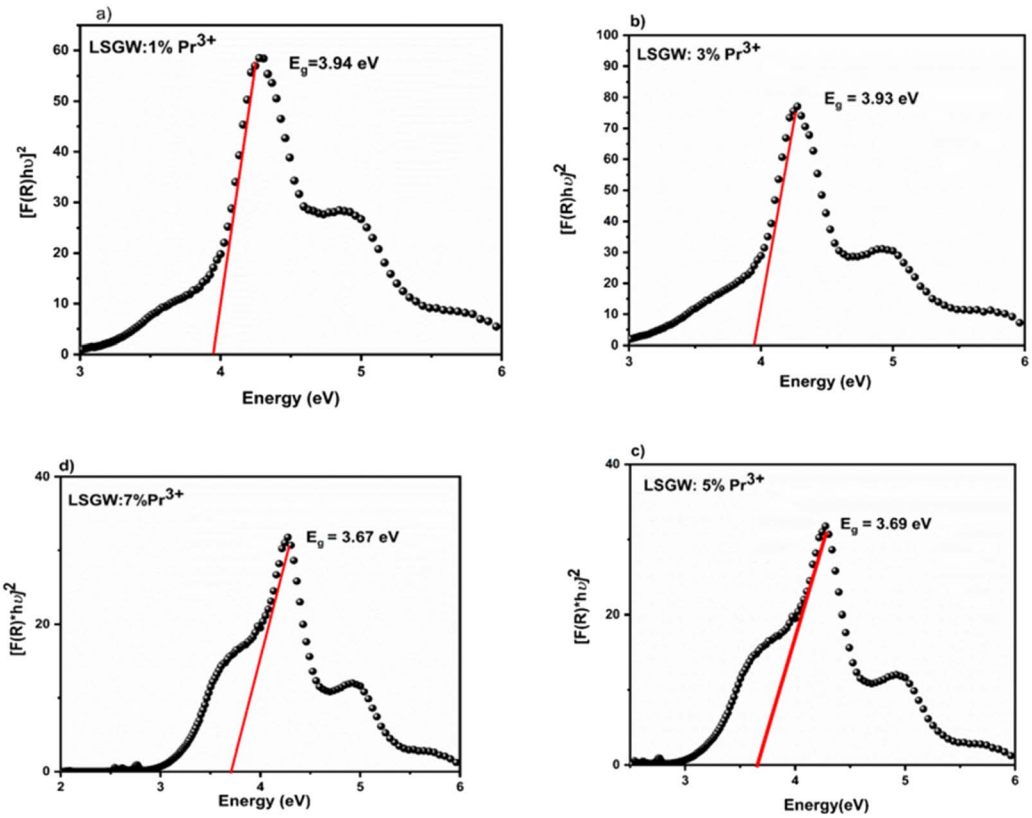

Fig. 5 The plot of $[F(R)h\nu]^2$ *versus* $h\nu$ of LSGW:*x*% Pr $^{3+}$ (a) $x = 1$ at%, (b) $x = 3$ at%, (c) $x =$ at. 5%, and (d) $x = 7$ at%.

and 595 nm which correspond to the $^3H_4 \rightarrow {}^3P_2$, $^3H_4 \rightarrow {}^3P_1 + {}^1I_6$, $^3H_4 \rightarrow {}^3P_0$ and $^3H_4 \rightarrow {}^1D_2$ electronic transitions, respectively.[37,38]

The Kubelka–Munk function is used to calculate the band gap of LSGW phosphors from diffuse reflectance spectra. The remission function establishes a link between the sample's diffuse reflectance (R), the absorption coefficient (K), and the diffusion coefficient (S) through the well known equation:[39]

$$F(R) = \frac{K}{S} = \frac{(1-R)^2}{2R} \quad (1)$$

Within the parabolic band structure, the energy band gap (E_g) can be obtained using the Tauc's relation given by the following equation:[39,40]

$$(F(R)h\nu)^2 = C(h\nu - E_g) \quad (2)$$

The value of E_g, which is approximately 3.69 eV, is calculated by extrapolating the right portion of the curve $(\alpha h\nu)^2$ from the $h\nu$ to zero curve. The allowable direct transition is characterized by nonlinear and linear sections in the plot of $[F(R)h\nu]^2$ as a function of $h\nu$. The linear portion describes the fundamental absorption, while the nonlinear section refers to a residual absorption involving states of impurities.

The energy gap values of LSGW:x at% Pr^{3+}, as illustrated in Fig. 5, were calculated to be: (a) $E_g = 3.94$ eV, (b) $E_g = 3.93$ eV, (c) $E_g = 3.69$ eV, and (d) $E_g = 3.67$ eV, for $x = 1$, 3, 5, and 7, respectively. The obtained results suggest that the incorporation of Pr^{3+} ions into the LSGW host induces a maximal variation of approximately 23 meV.

Theoretical simulation of Pr^3 free ion energy levels. Empirical energy levels for the free ion Pr^{3+} were derived from absorption and emission data gathered from LSGW:Pr^{3+}. These observed energy levels are summarized in Table 2. In addition, a theoretical energy diagram and corresponding eigenstates for Pr^{3+} were calculated using block diagonalization of the Hamiltonian's matrix in the basis set of coupled states $\langle 4f^2\rangle\langle 4f^2\tau SLJ\rangle$, considering intermediate coupling.

To optimize the model parameters, a MATLAB program implementing the Nelder–Mead simplex method[41] was used. The quality of the fit was assessed by the root mean square deviation (r.m.s.),[42,43] calculated using eqn (3):

Table 2 Experimental and theoretical energy level multiplets of free Pr^{3+} ion

	E_{Exp} (cm^{-1})	E_{The} (cm^{-1})		E_{Exp}	E_{The}
$^3H_4$	0	225.7	$^1D_2$	—	17 207.4
$^3H_5$	2320	2310.8	$^3P_0$	—	21 085.9
$^3H_6$	4492	4493.4	$^3P_1$	—	21 629.1
$^3F_2$	5131	5120.6	$^1I_6$	—	21 676.7
$^3F_3$	6494	6495.9	$^3P_2$	—	22 839.5
$^3F_4$	6966	6974.2	Conduction band: 29 842		
$^1G_4$	9962	9956.3	$^0S_0$	—	47 124.5

Table 3 Pr^{3+} free ion parameters[a]

F_2	F_4	F_6	α	β	γ	ζ
69 361	50 581	33 088	14.65	−423	1321	740.3

[a] $F_4 = 0.729248954 \times F_2$ and $F_6 = 0.477047309 \times F_2$.

$$\sigma = \left[\sum_i \frac{\left(E_i^{\exp} - E_i^{\text{calc}}\right)^2}{N - P}\right]^{1/2} \quad (3)$$

where N represents the total number of experimental data points and P indicates the number of free ion parameters. Key parameters such as Slater parameters F_2, F_4, and F_6, the spin–orbit coupling parameter ζ, and linear configuration interaction parameters α, β, and γ were obtained by fitting the theoretical and experimental energy levels for Pr^{3+}. These parameter values are presented in Table 3.

The agreement between the theoretical and experimental energy levels for Pr^{3+} was good, with a root mean square deviation of approximately 20 cm^{-1}. Table 3 shows the experimental and theoretical energy levels for Pr^{3+}. These results confirm that the theoretical model is consistent with the known energy levels of the $4f^2$ configuration for free Pr^{3+} ions, as well as ions embedded in various crystal lattices.[44]

The wave functions or the eigenstates are represented in the form:

$$|\Psi\rangle = \sum_{\alpha SL} C(\alpha SL)|\alpha SL\rangle \quad (4)$$

These eigenvectors associated with the praseodymium multiplets along with their intermediate coupling coefficients are calculated and presented in Table 4.

The free ion energy multiplets of rare-earth ions like Pr^{3+} determine the luminescence properties and their dependence on temperature. The way these energy levels are populated at different temperatures affects the intensity ratios used for temperature measurement and hence the sensitivity and accuracy of the luminescent thermometry. Understanding this relationship allows for the design of more effective phosphors for specific thermometric applications.

Photoluminescence spectroscopy

Luminescence of LSGW:Pr^{3+}. The excitation spectrum (PLE) of LSGW:Pr^{3+} phosphors monitored at the 648 nm emission band shown in Fig. 6a is in accordance with the results in UV-vis diffuse reflectance spectra. It exhibits two distinct regions: a relatively wide charge transfer band (CTB) in the 200–400 nm range, originating from the $(WO_4)^{2-}$ group,[36] and the 4f–4f intra-configurational transition bands specific to the Pr^{3+} ion, occurring between 450 and 486 nm. These peaks are attributed to the internal transitions of the $4f^2$ configuration of the Pr^{3+} ion, with the most intense emission observed at 450 nm attributed to the $^3H_4 \rightarrow {}^3P_2$ transition. Additionally, two other peaks are observed at 473 nm and 486 nm, corresponding to the $^3H_4 \rightarrow {}^3P_1 + {}^1I_6$ and $^3H_4 \rightarrow {}^3P_0$ transitions, respectively.[45] Fig. 6b displays the emission spectrum (PL) of LSGW:5 at% Pr^{3+} excited at 450 nm. The spectra exhibit several intense peaks resulting from intra-4f transitions. The most intense peak, appearing at 647 nm, is attributed to the $^3P_0 \rightarrow {}^3F_2$ transition. Other less intense peaks are observed at 487 nm, 531 nm, 557 nm, 603 nm, and 617 nm, 687, 708, and 731 corresponding to the transitions $^3P_0 \rightarrow {}^3H_4$, $^3P_1 \rightarrow {}^3H_5$, $^3P_0 \rightarrow {}^3H_5$, $^1D_2 \rightarrow {}^3H_4$, $^3P_0 \rightarrow {}^3H_6$, $^3P_1 \rightarrow {}^3H_5$, $^3P_1 \rightarrow {}^3F_4$ and $^3P_0 \rightarrow {}^3F_4$ respectively.[20,46,47] The energy level diagram and the possible optical transitions of Pr^{3+} ions in the LSGW host material are presented in Fig. 7.

To investigate the impact of Pr^{3+} doping concentration on LSGW in optical properties, we prepared a series of samples with different doping concentrations (x = 1, 3, 5, and 7 at%) under consistent conditions. Emission spectra of these samples were then recorded within the visible range of 450–750 nm under blue excitation (450 nm), as depicted in Fig. 8a. All emission spectra present the same shape with a variation of their intensities when increasing the Pr^{3+} concentration. It is clearly seen that the emission intensity of $^3P_0 \rightarrow {}^3F_2$ is more intense than that of $^3P_0 \rightarrow {}^3H_4$ at $x = 1$ at%. At a concentration of 3 at%, both transitions, $^3P_0 \rightarrow {}^3H_4$ and $^3P_0 \rightarrow {}^3F_2$ exhibit nearly identical emission intensities. However, with an increase in concentration to 5 at%, the emission intensity of the $^3P_0 \rightarrow {}^3H_4$ transition decreases while that of the $^3P_0 \rightarrow {}^3F_2$ transition increases. This result can be explained by the radiative energy

Table 4 Eigenstates of the Pr^{3+} ion in the LSGW host

	^3H	^3F	^1G	^1D	^3P	^1I	^0S
$^3H_4$	0.98618	−0.03002	0.16295				
$^3H_5$	1						
$^3H_6$	0.99857					−0.05351	
$^3F_2$		−0.98894		−0.14769	0.01330		
$^3F_3$		1					
$^3F_4$	−0.11858	−0.81478	0.56752				
$^1G_4$	0.11573	−0.57900	−0.80707				
$^1D_2$		0.14534		−0.94750	0.28481		
$^3P_0$					0.99539		0.09586
$^3P_1$					1		
$^1I_6$	0.05351					0.99857	
$^3P_2$		0.02946		−0.28360	−0.95849		
$^0S_0$					−0.09586		0.99539

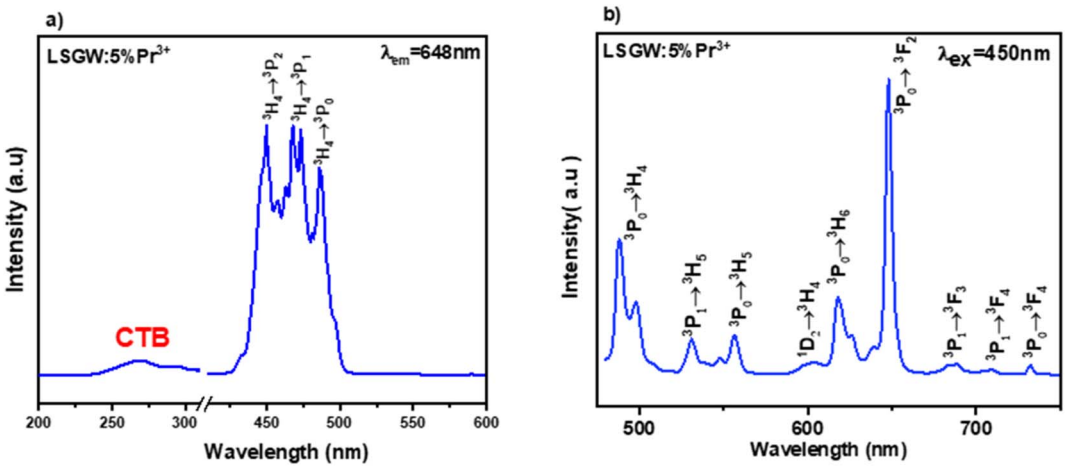

Fig. 6 (a) Excitation spectrum measured by monitoring the 648 nm emission band, and (b) emission spectrum excited at 450 nm of LSGW:5% Pr^{3+}.

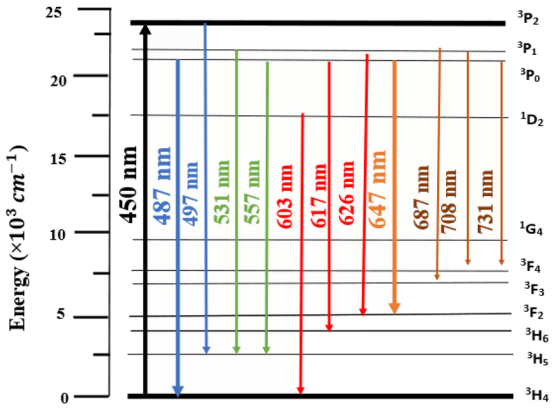

Fig. 7 Energy level diagram and the possible optical transitions of Pr^{3+} ion.

transfer between neighbouring luminescent centres of Pr^{3+} ions.[18] The highest intensity emission spectrum was attained at a doping concentration of 5 at%. Beyond this concentration, the emission intensity decreases due to the phenomenon of luminescence quenching or self-extinction. Generally, this quenching process is due to the short average distance between the Pr^{3+} ions. To investigate the main cause of concentration quenching, we use the eqn (5) provided by Blasse to estimate the critical distance between Pr^{3+} activator ions.[48]

$$R_c = 2\left(\frac{3V}{4\pi x_c N}\right)^{\frac{1}{3}} \quad (5)$$

where V is the volume of one-unit cell, N is the number of cationic sites for the dopant in a unit cell, and x_c is the critical concentration of the activator ion. In this case, $V = 322.31$, $N = 4$, and $x_c = 0.05$. Thus, the R_c value for energy transfer was calculated to be about 14.54 Å. This value is far greater than 5 Å for the exchange interaction. The concentration quenching mechanism of Pr^{3+} can be attributed to the electric multipole–multipole interactions. The energy transfer mechanism can be controlled by multipolar interactions according to Dexter theory[49] using the following formula:

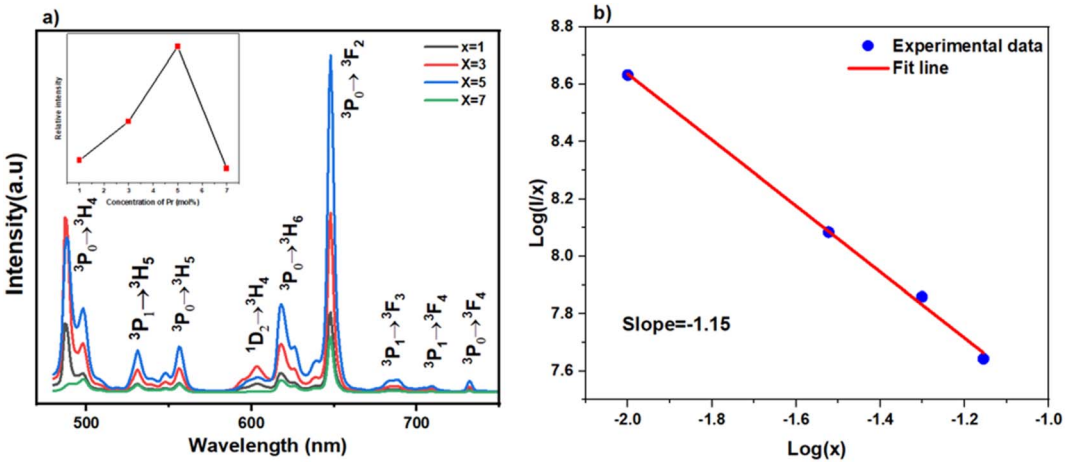

Fig. 8 (a) Emission spectra of LSGW:x at% Pr^{3+}(x = 1, 3, 5, and 7) excited at 450 nm, (b) plot of log(I/x) as a function of log(x).

$$\frac{1}{x} = k\left[1 + \beta(x)^{\frac{Q}{3}}\right]^{-1} \quad (6)$$

where k and β are constants, x value of dopant ion concentration greater than or equal to critical concentration, I is the emission intensity, and Q is multipolar interaction *i.e.*, 3 (exchange interaction), 6 (dipole–dipole), 8 (dipole–quadrupole), 10 (quadrupole–quadrupole). The variation of $\log(I/x)$ as a function of $\log(x)$ was presented in Fig. 8b, where I/x is the emission intensity per activator concentration. A linear line is obtained with a slope of −1.15 indicating that dipole–dipole interaction was responsible for the concentration quenching in LSGW:Pr^{3+} phosphors.

4. CIE chromaticity parameters

Fig. 9 shows the CIE chromaticity diagram for LSGW:x at% Pr^{3+} phosphors. It is clearly seen that the chromaticity coordinates of the compounds range from yellow to orange, with variation of the Pr^{3+} ions concentration. In order to find the practical utility of synthesized phosphors, the parameter Correlated Color Temperature (CCT) was calculated using the following formula proposed by McCamy:[50]

$$\mathrm{CCT} = -449n^3 + 3525n^2 - 6823n + 5520.33 \quad (7)$$

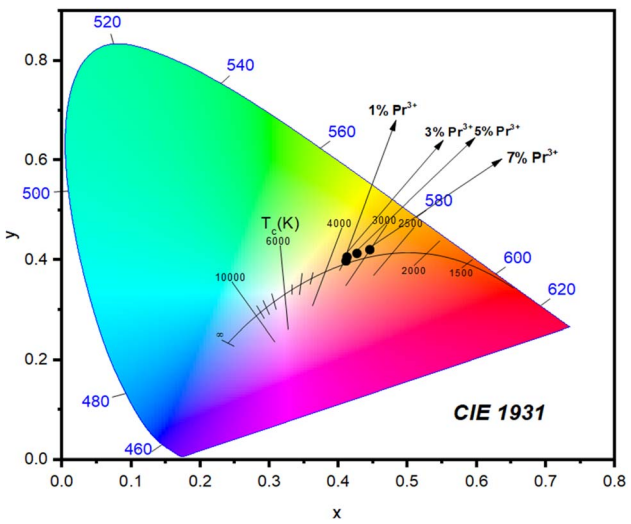

Fig. 9 CIE chromaticity diagram of LSGW:x% Pr^{3+} under 450 nm excitation.

Table 5 Chromaticity coordinates and TCC for LSGW:x% Pr^{3+}

Doping rate	x	y	CCT (K)
1 at%	0.41	0.39	3460
3 at%	0.41	0.41	3498
5 at%	0.43	0.41	3267
7 at%	0.44	0.42	3010

With $n = \dfrac{x - x_e}{y - y_e}$ representing the convergence epicentre, which is located at point (x_e = 0.3320 and y_e = 0.1858) on the chromaticity diagram. The chromaticity coordinates as well as the CCT values are listed in Table 5. The obtained CCT values are all below 5000 K, indicating that the LSGW:Pr^{3+} phosphor can be used in white light-emitting diodes.

5. Luminescent thermometry

In order to investigate the temperature effect, the temperature-dependent PL spectra of LSGW:5% Pr^{3+} were recorded from 300 to 440 K, under 450 nm excitation, as shown in Fig. 10. Notably, all emission spectra exhibit consistent spectral shapes, with no discernible shifts in peak position or full-width at half-maximum, indicating uniform distribution of crystal field. However, it is found that temperature has varying effects on emission-line intensity. Particular emphasis should be placed on transitions from thermally coupled $^3P_0(I_1)$ and $^3P_1(I_2)$ excited levels. In Fig. 11, the integrated intensities of $^3P_1 \rightarrow {}^3H_5$ (531 nm), $^3P_0 \rightarrow {}^3H_5$ (557 nm) and $^3P_0 \rightarrow {}^3H_6$ (617 nm) are depicted against temperature variation. Notably, the emission intensity of the higher energy transition ($^3P_1 \rightarrow {}^3H_5$) increases, while the intensities of the lower-energy transitions ($^3P_0 \rightarrow {}^3H_5$ and $^3P_0 \rightarrow {}^3H_6$) decrease as temperature increased, following a Boltzmann type distribution:[21]

$$\mathrm{LIR} = \frac{I_2}{I_1} = B\exp\left(-\frac{\Delta E}{k_B T}\right) \quad (8)$$

where LIR is the luminescence intensity ratio of the emission bands, T is the absolute temperature, B is a constant, k_B = 0.695 cm^{-1} K^{-1} is the Boltzmann constant, and ΔE is the energy gap between the two thermally coupled levels $^3P_0$ and $^3P_1$.

The temperature dependence of LIR between (I_{531} and I_{557}) and (I_{531} and I_{617}) relative to the temperature range 300–440 K are plotted in Fig. 12a and b, respectively. The experimental data are well fitted using eqn (1). The effective energy difference

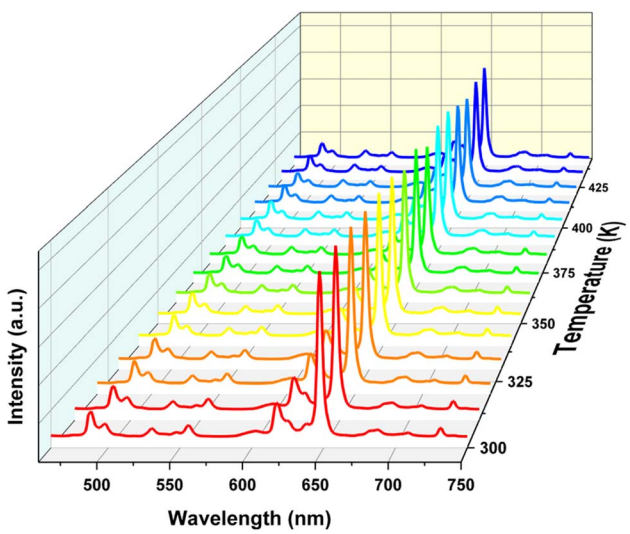

Fig. 10 Emission spectra of LSGW:5% Pr^{3+} in the 300–440 K range upon 450 nm excitation.

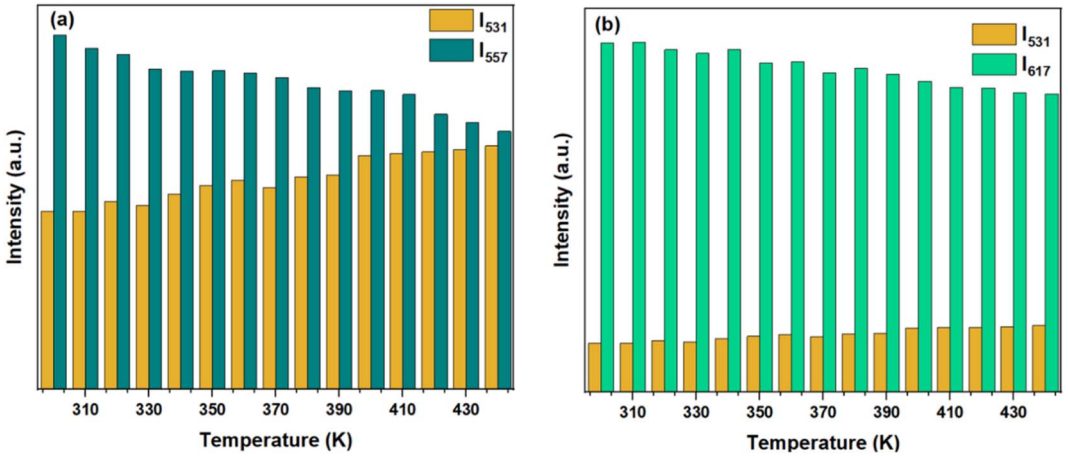

Fig. 11 Histogram displaying the integrated intensity of (a) $^3P_1 \rightarrow {}^3H_5$ (531 nm) and $^3P_0 \rightarrow {}^3H_5$ (557 nm) and (b) $^3P_1 \rightarrow {}^3H_5$ (531 nm) and $^3P_0 \rightarrow {}^3H_6$ (617 nm) emissions in the range of temperature from 300 to 440 K.

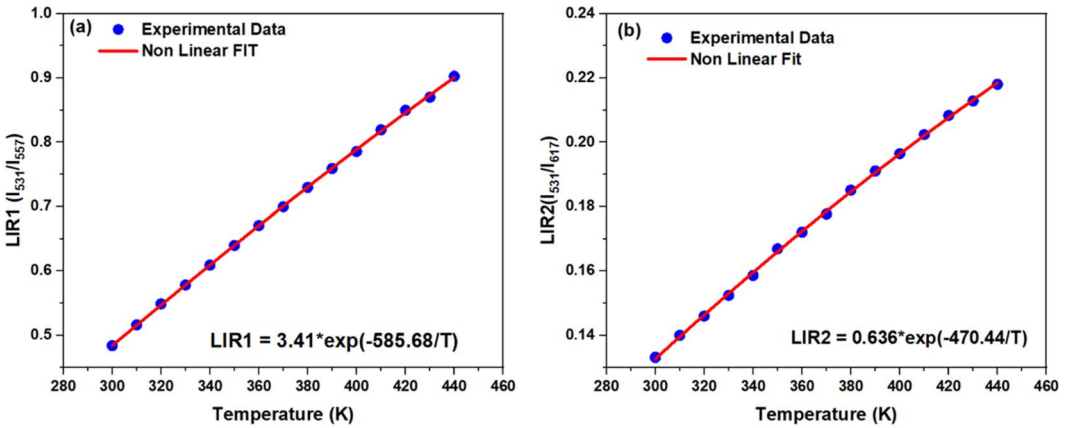

Fig. 12 (a) The temperature dependent LIR1 (I_{531}/I_{557}) and (b) LIR2 (I_{531}/I_{617}) in 300–440 K temperature range.

between the thermally coupled levels obtained from the fitting for LIR1 (I_{531}/I_{557}) is 403 cm^{-1}, and for LIR2 (I_{531}/I_{617}), it is 324 cm^{-1}. These values closely match the ΔE between the $^3P_1$ and $^3P_0$ states, which is approximately 500 cm^{-1}.[19] The most important parameters for temperature sensing applications are the absolute (S_a) and the relative thermal sensitivities (S_r) defined as follows:[51]

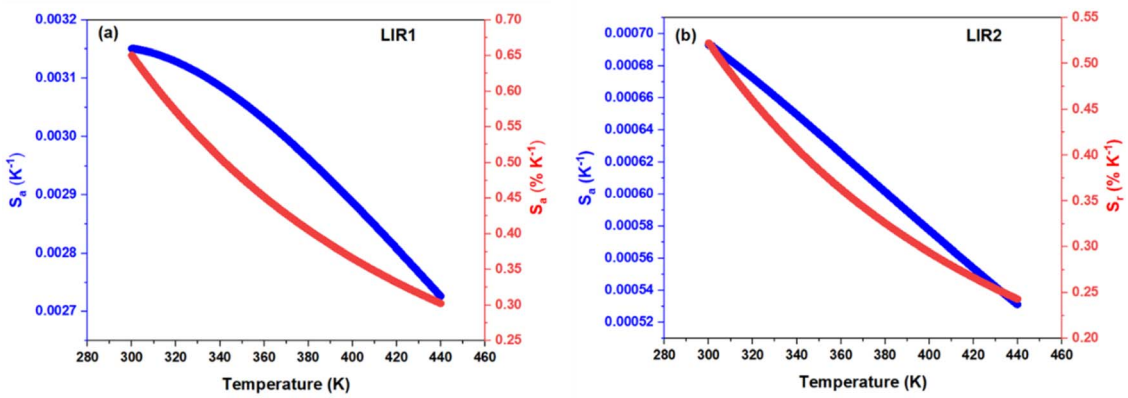

Fig. 13 S_a and S_r values in the 300–440 K temperature range corresponding to (a) LIR1 (I_{531}/I_{557}) and (b) LIR2 (I_{531}/I_{617}).

$$S_a = \frac{\partial \mathrm{LIR}}{\partial T} \quad (9)$$

$$S_r = \frac{1}{\mathrm{LIR}} \times \frac{\partial \mathrm{LIR}}{\partial T} \times 100\% \quad (10)$$

Fig. 13 shows the variation of S_a and S_r of the LSGW:Pr^{3+} phosphor as a function of temperature from 300 to 440 K. For LIR1 and LIR2 the S_a and S_r values decrease with temperature, and they take the maximum value at room temperature (300 K).

Table 6 Maximum relative thermal sensitivity of Pr^{3+} based luminescent thermometers using the luminescence intensity ratio

Phosphors	S_r (% K^{-1})	Temperature range (K)	References
$SrMoO_4$:Pr^{3+}	0.45 (I_{486}/I_{601})	298–498	17
$Na_2La_2Ti_3O_{10}$:Pr^3	1.96 (I_{611}/I_{491})	303–543	52
Lu_2GeO_5:Pr^{3+}	1.12 (I_{490}/I_{608})	150–550	53
$CaSc_2O_4$:Pr^{3+}	2.49 (I_{360}/I_{630})	275–490	55
Gd_2ZnTiO_6:Pr^{3+}	1.67 (I_{617}/I_{492})	293–433	56
YVO_4:Pr^{3+}	0.78 (I_{595}/I_{618})	303–323	57
$CaMoO_4$:Pr^{3+}	0.96 (I_{605}/I_{490})	303–573	58
$LiSrGd(WO_4)_3$:Pr^{3+}	0.65 (I_{531}/I_{557})	300–440	This work
	0.52 (I_{531}/I_{617})		

The maximal absolute and relative thermal sensitivities were found to be 0.00315 K^{-1}, and 0.65% K^{-1} for LIR1 and 0.0007 K^{-1} and 0.52% K^{-1} for LIR2. Table 6 shows the comparison of the S_r values for different materials doped with Pr^{3+} ions in different temperature ranges.

In the field of luminescent thermometry, $LiSrGd(WO_4)_3$:Pr^{3+} phosphors present a balanced performance in comparison to several other notable hosts. With a relative sensitivity (S_r) of 0.65% K^{-1} (I_{531}/I_{557}) and 0.52% K^{-1} (I_{531}/I_{617}), $LiSrGd(WO_4)_3$:Pr^{3+} exhibits moderate sensitivity values, outperforming $SrMoO_4$:Pr^{3+} (S_r = 0.45% K^{-1})[17] but falling behind more sensitive hosts like $Na_2La_2Ti_3O_{10}$:Pr^{3+} (S_r = 1.96% K^{-1}).[52]

The temperature range of 300–440 K for $LiSrGd(WO_4)_3$:Pr^{3+} is narrower than that of Lu_2GeO_5:Pr^{3+} (150–550 K),[53] yet it remains sufficient for various practical applications. These applications include biomedical diagnostics where the physiological temperature range is critical, microelectronics for real-time temperature monitoring of components, industrial processes requiring precise temperature control, environmental monitoring, household appliances for enhanced safety and efficiency, and energy systems such as battery management in electric vehicles and thermal management in solar panels.[5,17,54] Additionally, the specific intensity ratios (I_{531}/I_{557} and I_{531}/I_{617}) used by $LiSrGd(WO_4)_3$:Pr^{3+} offer unique advantages for precise

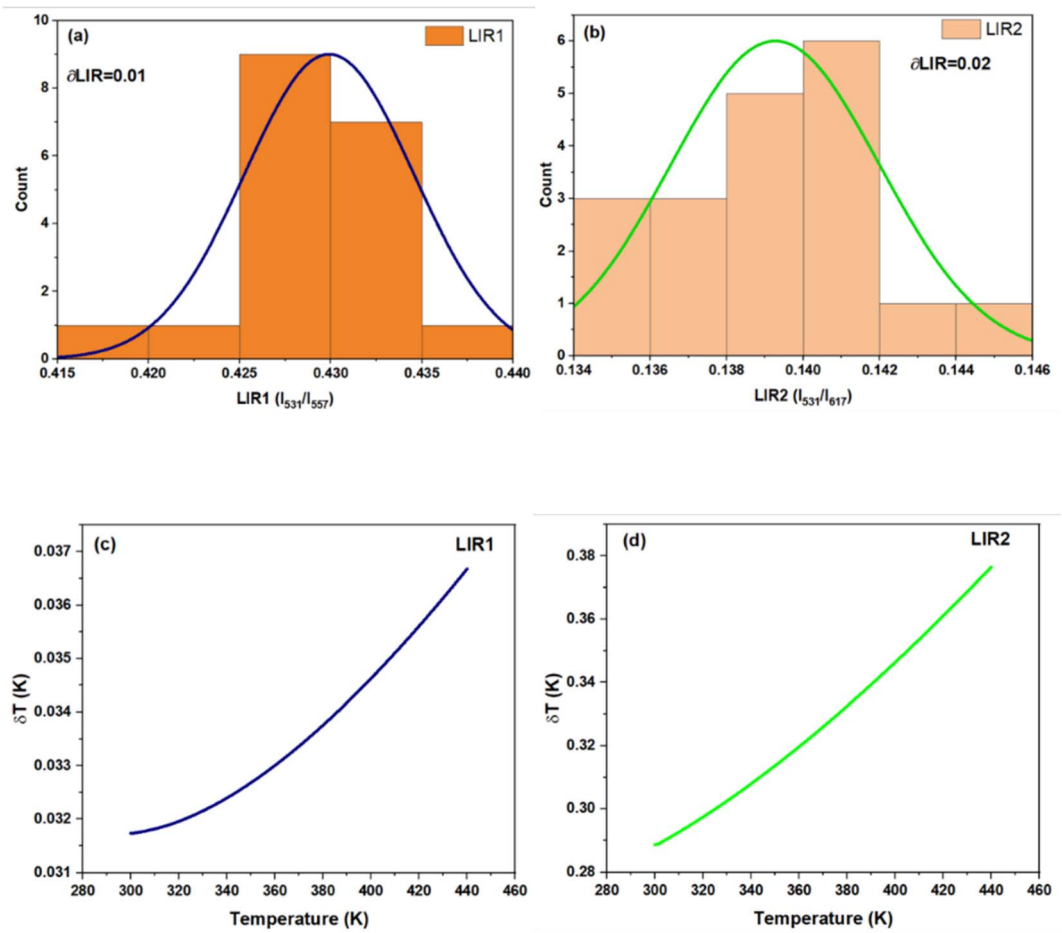

Fig. 14 Value of ∂LIR/LIR obtained using 20 measurements at 298 K of (a) LIR1 and (b) LIR2 and (c and d) temperature uncertainty values δ*T*.

temperature sensing, similar to the specialized ratios utilized by other phosphors. Although $CaSc_2O_4$:Pr^{3+} ($S_r = 2.49\%\ K^{-1}$)[55] and Gd_2ZnTiO_6:Pr^{3+} ($S_r = 1.67\%\ K^{-1}$)[56] demonstrate higher sensitivities, $LiSrGd(WO_4)_3$:Pr^{3+} provides a reliable alternative with its balanced sensitivity and adequate temperature range. This makes it a valuable candidate for luminescent thermometry applications, offering a practical solution with moderate sensitivity and a suitable operational temperature range.

In addition to having high sensing sensitivity, the performance of a thermometer must also be assessed based on its temperature resolution, which determines the precision of the temperature measurements. The temperature uncertainty (δT) value can be determined through various experimental methods: by measuring a series of emission spectra at the same temperature, using the temperature calibration curve, or monitoring the cooling of the sample.[59] In this work, δT was obtained using the first method with the following expression:[60]

$$\delta T = \frac{1}{S_r}\frac{\partial \mathrm{LIR}}{\mathrm{LIR}} \quad (11)$$

where ∂LIR/LIR is the sensitivity of the detection system. In this case, ∂LIR signifies the standard deviation of the LIR data obtained from multiple measurements at a constant temperature, while LIR refers to the mean value of these measurements. To evaluate the sensitivity of the detection system, we performed 20 LIR measurements of our phosphor at room temperature, as depicted in the histograms in Fig. 14a and b. The estimated δT values increase with temperature and still below 1 K (Fig. 14c and d) which confirms the good thermometric performance of the LSGW:Pr^{3+} phosphor.

6. Conclusion

This study successfully synthesized $LiSrGd(WO_4)_3$ (LSGW) phosphors doped with Pr^{3+} using the solid-state method, confirming their potential for optical thermometry. Structural analyses verified Pr^{3+} incorporation with minimal bandgap alteration. Optimal doping (5 at%) yielded the highest emission intensity, while quenching effects at higher concentrations were attributed to dipole–dipole interactions. The LIR method demonstrated high sensitivity ($S_a = 31.5\ 10^{-4}\ K^{-1}$, $S_r = 0.65\%\ K^{-1}$ at 300 K) and low temperature uncertainty ($\delta T < 1$ K) across 300–440 K, highlighting the competitive performance of LSGW:Pr^{3+} compared to similar materials. These findings establish LSGW:Pr^{3+} phosphors as promising candidates for precise and reliable optical temperature sensing.

Data availability

All data underlying the results are available as part of the article and no additional source data are required.

Conflicts of interest

There are no conflicts to declare.

References

1 V. Lojpur, M. G. Nikolić, D. Jovanović, M. Medić, Ž. Antić and M. D. Dramićanin, *Appl. Phys. Lett.*, 2013, **103**, 141912.
2 K. Li, M. Shang, H. Lian and J. Lin, *J. Mater. Chem. C*, 2016, **4**, 5507–5530.
3 X. Wang, Q. Liu, Y. Bu, C. S. Liu, T. Liu and X. Yan, *RSC Adv.*, 2015, **5**, 86219–86236.
4 I. E. Kolesnikov, A. A. Kalinichev, M. A. Kurochkin and E. Y. Kolesnikov, *Mater. Des.*, 2019, **184**, 108188.
5 M. Runowski, P. Wozny, I. R. Martín, V. Lavín and S. Lis, *J. Lumin.*, 2019, **214**, 116571.
6 B. del Rosal, D. Ruiz, I. Chaves-Coira, B. H. Juarez, L. Monge, G. Hong, N. Fernandez and D. Jaque, *Adv. Funct. Mater.*, 2018, **28**, 1806088.
7 D. Jaque and F. Vetrone, *Nanoscale*, 2012, **4**, 4301–4326.
8 E. C. Ximendes, U. Rocha, T. O. Sales, N. Fernández, F. Sanz-Rodríguez, I. R. Martín, C. Jacinto and D. Jaque, *Adv. Funct. Mater.*, 2017, **27**, 1702249.
9 M. Runowski, A. Shyichuk, A. Tymiński, T. Grzyb, V. Lavín and S. Lis, *ACS Appl. Mater. Interfaces*, 2018, **10**, 172691–177279.
10 S. F. León-Luis, U. R. Rodríguez-Mendoza, E. Lalla and V. Lavín, *Sens. Actuators, B*, 2011, **158**, 208–213.
11 Z. Liu and R. X. Wang, *Chalcogenide Lett.*, 2022, **19**, 471–481.
12 W. Ye, C. Ma, Y. Li, C. Zhao, Y. Wang, C. Zuo, Z. Wen, Y. Li, X. Yuan and Y. Cao, *J. Mater. Chem. C*, 2021, **9**, 15201–15211.
13 C. D. S. Brites, K. Fiaczyk, J. F. C. B. Ramalho, M. Sójka, L. D. Carlos and E. Zych, *Adv. Opt. Mater.*, 2018, **6**, 1701318.
14 S. S. Zhou, G. C. Jiang, X. T. Wei, C. K. Duan, Y. H. Chen and M. Yin, *J. Nanosci. Nanotechnol.*, 2014, **14**, 3739–3742.
15 Y. Huang, L. Luo, J. Wang, Q. Zuo, Y. Yao and W. Li, *J. Appl. Phys.*, 2015, **118**, 044101.
16 M. S. Pudovkin, S. L. Korableva, D. A. Koryakovtseva, E. V. Lukinova, A. V. Lovchev, O. A. Morozov and V. V. Semashko, *J. Nanopart. Res.*, 2019, **21**, 2–14.
17 L. Li, P. Yang, W. Xia, Y. Wang, F. Ling, Z. Cao, S. Jiang, G. Xiang, X. Zhou and Y. Wang, *Ceram. Int.*, 2021, **47**, 769–775.
18 X. Tian, J. Li, H. Sheng, T. Li, L. Guo, C. Ji, Z. Huang, J. Wen, X. Liu, C. Li, J. Li and Y. Peng, *Ceram. Int.*, 2022, **48**, 3860–3868.
19 M. S. Pudovkin, O. A. Morozov, V. V. Pavlov, S. L. Korableva, E. V. Lukinova, Y. N. Osin, V. G. Evtugyn, R. A. Safiullin and V. V. Semashko, *J. Nanomater.*, 2017, **2017**, 3108586.
20 S. Jana, A. Mondal, J. Manam and S. Das, *J. Alloys Compd.*, 2020, **821**, 153342.
21 M. Runowski, P. Woźny, I. R. Martín, V. Lavín and S. Lis, *J. Lumin.*, 2019, **214**, 116571.
22 H. Zhang, Z. Gao, G. Li, Y. Zhu, S. Liu, K. Li and Y. Liang, *Chem. Eng. J.*, 2020, **380**, 122491.
23 B. Han, Y. Dai, J. Zhang, B. Liu and H. Sh, *Ceram. Int.*, 2018, **44**, 3734–3740.
24 K. Zhong, H. Ye, X. Wang, Y. Li and X. Yao, *J. Mater. Sci.: Mater. Electron.*, 2021, **32**, 17170–17181.

25 Q. Liu, X. Li, B. Zhang, L. Wang, Q. Zhang and L. Zhang, *Ceram. Int.*, 2016, **42**, 15294–15300.
26 L. Fan, Y. X. Fan, Y. H. Duan, Q. Wang, H. T. Wang, G. H. Jia and C. Y. Tu, *Appl. Phys. B*, 2009, **94**, 553–557.
27 A. K. Parchur and R. S. Ningthoujam, *Dalton Trans.*, 2011, **40**, 7590–7594.
28 J. Bi, L. Wu, Y. Zhang, Z. Li, J. Li and X. Fu, *Appl. Catal., B*, 2009, **91**, 135–143.
29 J. Yu, L. Qi, B. Cheng and X. Zhao, *J. Hazard. Mater.*, 2008, **160**, 621–628.
30 F. Ayachi, K. Saidi, M. Dammak, J. J. Carvajal and M. Cinta Pujol, *RSC Adv.*, 2024, **14**, 13494–13504.
31 S. Ward, M. A. Isaacs, G. Gupta, M. Mamlouk and S. S. Pramana, *Sustainable Energy Fuels*, 2021, **5**, 154–165.
32 M. P. Selvam and K. J. Rao, *Adv. Mater.*, 2000, **12**, 1621–1624.
33 M. Song, W. Zhao, W. Ran, J. Xue, Y. Liu and J. H. Jeong, *J. Alloys Compd.*, 2019, **803**, 1063–1074.
34 L. Macalik, J. Hanuza and A. A. Kaminskii, *J. Raman Spectrosc.*, 2002, **33**, 92–103.
35 A. H. Ahmad and A. K. Arof, *lonics*, 2004, **10**, 200–205.
36 P. F. S. Pereira, I. C. Nogueira, E. Longo, E. J. Nassar, I. L. V. Rosa and L. S. Cavalcante, *J. Rare Earths*, 2015, **33**, 113.
37 P. Nemec, B. Frumarová and M. Frumar, *J. Non-Cryst. Solids*, 2000, **270**, 137.
38 M. Laroche, A. Braud, S. Girard, J. L. Doualan, R. Moncorge, M. Thuau and L. D. Merkle, *J. Opt. Soc. Am. B*, 1999, **16**, 2269.
39 A. E. Morales, E. S. Mora and U. Pal, *Rev. Mex. Fis. S*, 2007, **53**, 18.
40 L. L. Noto, M. L. Chitambo, O. M. Ntwaeaborwa and H. C. Swart, *Powder Technol.*, 2013, **247**, 147–150.
41 J. A. Nelder and R. Mead, *Comput. J.*, 1965, **7**, 308.
42 K. Rajnak, *J. Chem. Phys.*, 1965, **43**, 847.
43 K. M. Murdoch, N. M. Edelstein, L. A. Boatner and M. M. Abraham, *J. Chem. Phys.*, 1996, **105**, 2539.
44 M. L. Duan, X. F. Yang and J. H. Li, *Adv. Mater. Res.*, 2011, **418–420**, 665–669.
45 C. Basavapoornima, T. Maheswari, C. R. Kesavulu, W. Pecharapa, J. Kaewkhao and C. K. Jayasankar, *AIP Conf. Proc.*, 2020, **2279**, 060002.
46 M. Runowskia, P. Woznya, I. R. Martínb, V. Lavínb and S. Lisa, *J. Lumin.*, 2019, **214**, 116571.
47 M. Fhoula, K. Saidi and M. Dammak, *J. Alloys Compd.*, 2024, **979**(5), 173537.
48 G. Blasse and B. C. Grabmaier, *Luminescent Materials*, Springer-Verlag, 1994.
49 D. L. Dexter and J. H. Schulman, *J. Chem. Phys.*, 1954, **22**, 1063–1070.
50 C. S. McCamy, *Color Res. Appl.*, 1992, **17**, 142–144.
51 I. E. Kolesnikov, A. A. Kalinichev, M. A. Kurochkin, D. V. Mamonova, E. Y. Kolesnikov and E. Lahderanta, *J. Phys. Chem. C*, 2019, **123**, 5136–5143.
52 Y. Gao, F. Huang, H. Lin, J. Xu and Y. Wang, *Sens. Actuators, B*, 2017, **243**, 137–143.
53 M. Sójka, C. D. S. Brites, L. D. Carlos and E. Zych, *J. Mater. Chem. C*, 2020, **8**, 10086–10097.
54 S. Kaur, H. Kaur, A. S. Rao and G. V. Prakash, *Phys. B*, 2024, **690**, 416224.
55 S. Wang, S. Ma, G. Zhang, Z. Ye and X. Cheng, *ACS Appl. Mater. Interfaces*, 2019, **11**, 42330–42338.
56 Y. Gao, Y. Cheng, T. Hu, Z. Ji, H. Lin, J. Xu and Y. Wang, *J. Mater. Chem. C*, 2018, **6**, 11178–11183.
57 H. Zhou, W. Gao, P. Cai, B. Zhang and S. Li, *Solid State Sci.*, 2020, **104**, 106283.
58 X. Tian, S. Xu, J. Wen, L. Zhu, C. Ji, Z. Huang, X. Wang, F. Luo, X. Liu, Y. Lu, J. Li, C. Li, Y. Peng, J. Cao and Z. He, *Ceram. Int.*, 2023, **49**, 27126–27137.
59 I. E. Kolesnikov, D. V. Mamonova, M. A. Kurochkin, E. Y. Kolesnikov and E. Lahderanta, *ACS Appl. Nano Mater.*, 2021, **4**, 1959–1966.
60 J. Stefanska and L. Marciniak, *Adv. Photonics Res.*, 2021, **2**, 2100070.